HST/NICMOS spectroscopy of Charon's leading and trailing hemispheres

Christophe Dumas and Richard J. Terrile

Jet Propulsion Laboratory, California Institute of Technology, Mail Stop 183-501, 4800 Oak Grove Drive, Pasadena, CA 91109

Robert H. Brown

University of Arizona, Lunar and Planetary Laboratory, Tucson, AZ 85721

Glenn Schneider

University of Arizona, Steward Observatory, 933 N. Cherry Avenue, Tucson, AZ 85721

and

Bradford A. Smith

University of Hawaii, Institute for Astronomy, 2680 Woodlawn Dr., Honolulu, HI 96822

Received _____; accepted _____

ABSTRACT

We used the near-infrared camera and multiobject spectrometer NICMOS on the Hubble Space Telescope to obtain [1.1–2.4]μm, low-resolution (R$\sim$200) slitless grism spectrophotometry of the individual members of the Pluto-Charon system. Water ice is present in its crystalline state on both leading and trailing hemispheres of Charon. A 2.21μm absorption band is detected in the reflectance spectrum of its leading side only. Geological activity on Charon or, more likely, implantation of ions escaped from Pluto's atmosphere, could account for the formation of species like ammonia hydrate ($NH_3 \cdot H_2O$) locally on the satellite. We also measured a slightly higher geometric albedo for Charon than reported from the mid-80's observations of the mutual events.

Subject headings: satellites: Charon, near-infrared spectroscopy, surface composition, ices

1. Introduction

Although Pluto's discovery was made seventy years ago, most of the information we have collected on its surface composition has only been obtained very recently. Sensitive telescope instrumentation is now available to carry out spectrophotometric observations of the Pluto-Charon system at visible, and particularly at near-infrared wavelengths, a spectral range that provides an excellent diagnostic of the physical state of the ices present on the surface. The surface of Pluto was first suggested to be primarily covered with methane ice (Cruikshank *et al.* 1976). Additional photometric observations, carried-out at various rotational phases (Buie and Fink 1987), showed that methane is not distributed uniformly over the surface. Owen *et al.* (1993) reported that N_2 ice is in fact the most abundant compound on Pluto, followed by CH_4 and CO. Currently, the planet is moving away from the sun and its atmosphere is slowly condensing on the surface (Stern *et al.* 1988). While N_2 gas should also be the main constituent of Pluto's atmosphere (Owen *et al.* 1993), only methane gas has already been detected from the $2\nu_3$ band at 1.67μm (Young *et al.* 1997) and CO gas awaits detection. Pluto's surface displays patches of bright N_2 rich-regions and dark nitrogen-depleted areas (Jewitt 1994). N_2 ice may be concentrated in the polar regions at temperatures $\leq$ 40K (Tryka *et al.* 1994), while ices with lower volatility should cover the equatorial regions. The surface temperature varies locally and recent ISO measurements (Lellouch *et al.* 1998) confirmed the presence of cold/bright and warm/dark regions. The visible albedo distribution across Pluto was determined from lightcurve inversion techniques (Buie *et al.* 1992, Young *et al.* 1999) and direct imaging using HST/FOC (Stern *et al.* 1997). Both methods confirmed the presence of bright polar regions while the equatorial zone displays a darker but highly variegated surface.

Due to the small angular separation between Pluto and its satellite (from 0.3" to 0.9"),

our knowledge of Charon's surface composition could, until recently, only be deduced from the analysis of the mid-80's occultation events. These observations showed that Charon is mostly covered with H_2O ice (Buie *et al.* 1987, Marcialis *et al.* 1987, Fink and DiSanti 1988). Later analysis by Roush (1994) and Roush *et al.* (1996) of the mid-80's photometric measurements suggested that the surface of Charon could also be covered with patches of CO_2 ice mixed with large grained CH_4 ice in addition to H_2O. Dumas *et al.* (1999) reported HST/NICMOS observations revealing for the first time the crystalline state of water ice over Charon. This result was confirmed by independent HST/NICMOS observations of Charon made by Buie and Grundy (2000) as well as by ground-based observations carried-out at Keck Observatory by Brown and Calvin (2000). Brown and Calvin (2000) also reported the presence of a 2.21μm band in their spectrum of Charon which they attributed to the presence of ammonia ice on the surface.

This paper presents the results of a reanalysis of the HST/NICMOS observations obtained by Dumas *et al.* (1999). We confirm the presence of a 2.21μm absorption feature in the spectrum of Charon, however this absorption appears to be present in the spectrum of the leading hemisphere of Charon only. This result suggests that resurfacing processes, possibly involving Pluto, are currently occurring on Charon. A mechanism is discussed, which involves bombardment of Charon's surface by ions escaping from Pluto's atmosphere.

2. Observations

We report spectroscopic observations of the Pluto-Charon system obtained in 1998 on June 11 and June 14 (HST GTO/7223 program) at Charon's maximum elongation using the Hubble Space Telescope (HST) and its Near-Infrared Camera and Multi-Object Spectrometer NICMOS (Thompson *et al.* 1998). The details of the geometry of the

Pluto-Charon system are described in Table 1. Planetocentric coordinates were calculated for both dates using the 1994 IAU model (Davies *et al.* 1996).

EDITOR: PLACE TABLE 1 HERE.

NICMOS has three 256x256 HgCdTe low-noise detectors covering a [0.8-2.4]μm spectral range with pixel scale ranging from 43mas/pixel (camera 1) to 203mas/pixel (camera 3). Camera 3 (NIC3) is equipped with a set of 3 grisms (G096, G141, G206) providing low resolution (R$\sim$200) slitless spectrophotometric capabilities. In this paper we discuss the results obtained using NIC3 and the G141 and G206 grisms, spanning a spectral range from 1.1μm to 2.4μm. Though NIC3 normally produces slightly afocal images, our data were obtained during the June 1998 "Camera-3 campaign" when the HST secondary mirror was adjusted to achieve optimal optical performance. Pluto and Charon were separated by 0.9" for the dates of our observations. However, due to HST scheduling constraints, the line joining the binary system could not be oriented perpendicular to the dispersion direction hence the spatial separation of the spectra was reduced to 0.5" (Table 1). Table 2 summarizes the exposure parameters for the G141 and G206 grisms. Because the wavelength solution of each spectrum is a function of the position of the science target on the detector, we initially obtained an image of Pluto-Charon through the F150W broad filter. Two spectra of Pluto-Charon (320 seconds per exposure) were then recorded with the G141 grism. A small telescope offset was implemented between each exposure to collect data from different locations on the detector and to reduce the contamination of our data from flat-field residual effects, as well as to sample around bad pixels. The last step was to acquire the long-wavelength spectra using the G206 grism. Because the G206 background level was $\sim$ 150 times higher than for the G141 grism, shorter exposures were required to avoid saturation. We recorded a series of 12 spectra (64 seconds each) at four different

locations on the detector (3 images per position of the telescope).

EDITOR: PLACE TABLE 2 HERE.

3. Data reduction

The extraction and absolute photometric calibration of the spectra of Pluto and Charon were achieved using the "Nicmoslook" software (Pirzkal and Freudling 1998, McCarthy *et al.* 1999) developed at ST-ECF for reduction of the NICMOS spectroscopic data. The first step in data-reduction was to subtract the background from the G206 images. The background was estimated from a median combination of the set of 4-position dithered G206 images. The low background level for the G141 grism was simply fitted during the extraction. Because the spectra of the two objects partially overlap, we estimated their individual contributions and created, for each original spectrum, two images containing separate synthetic spectra of Pluto and Charon. Figure 1 shows the result of fitting the contribution of Pluto and Charon along one detector column. Because the 0.2"/pixel scale of NIC3 oversamples the Point Spread Function (PSF), each image was first rebinned to a finer grid (rebin factor = 8) via bi-cubic convolution interpolation (Park and Schowengerdt 1983). The angle of dispersion of the spectra with respect to the detector horizontal axis was measured as well as the location where the spectrum was illuminating the exact center of one pixel. From the knowledge of these two parameters, we could estimate the width of Pluto and Charon's PSFs. The separated synthetic spectra of Pluto and Charon were obtained by adjusting the amplitude and position of the two PSFs in order to minimize the variance of the difference between the original and synthetic profiles (Fig. 1). This measurement was made over the range of pixels covered by the two objects and a good fit was reached after only 3 iterations. The process returned two images corresponding to the

separated spectra of Charon and Pluto which were rebinned back to the original resolution. The maximum count rate for Pluto in a single G206 exposure was near 330 e^-/s while the residual count rate was in the ± 13 e^-/s range (NIC3 gain = $6.5e^-$/ADU). The residual image (*original image* − *synthetic image*) was used to improve the models of Pluto and Charon spectra. The total flux ($\mathcal{F}_T$) in a detector pixel due to Pluto ($\mathcal{F}_P$) and Charon ($\mathcal{F}_C$) is simply $\mathcal{F}_T = \mathcal{F}_P + \mathcal{F}_C$, and the residual value for one particular pixel is $res = \mathcal{F}_{Orig} - \mathcal{F}_T$, where $\mathcal{F}_{Orig}$ is the flux of the original image for this pixel. Then the corrected fluxes for the fits of Pluto and Charon are respectively $F'_P = F_P + \frac{F_P}{F_T} \times res$, and $F'_C = F_C + \frac{F_C}{F_T} \times res$. This correction performed individually for all pixels, allows us to conserve the original total flux of Pluto and Charon while correcting the models for the uncertainties in the individual pixel response and the exact position of the PSF *wrt* the center of the pixel.

EDITOR: PLACE FIGURE 1 HERE.

At this stage, the data have been processed in a way that we can extract and photometrically calibrate the G141 and G206 spectra of Pluto and Charon. Version 2.9.2 of Nicmoslook (Freudling and Pirzkal 1998, Pirzkal and Freudling 1998) was used for this purpose. The wavelength solution for all NICMOS grisms as a function of the position of the object on the detector has been parameterized. The only adjustment we made consisted of accounting for the planet's apparent motion which had the effect of modifying the original position measured from the F150W image. The NICMOS detectors do not have spatially flat responses across their pixels. Thus, the flux measured in an undersampled pixel depends upon the location of the PSF core *wrt* the pixel center. It was therefore necessary to extract the spectra using a model of the Intra Pixel Response Function (IPRF) (see Lauer 1999 for a detailed description of the IPRF). The average effect of the IPRF was larger for "Camera-3 campaign" observations than for observations carried-out when the PSF was not exactly in focus for NIC3. Similarly, because the PSF is better sampled at

longer wavelengths, the correction for the G206 grism data was smaller than for the G141 grism. We used the observations of the solar analog P330E collected during the June 1998 "Camera-3 campaign" (HST 7959 program) to determine the amplitude of a characteristic IPRF correction to apply to our G206 and G141 spectra. The scatter of the data points was measured before and after applying the IPRF correction. For this purpose, we defined the mean spectrum for each grism and subtracted it from the individual spectra to calculate the means of the standard deviations over a defined range of wavelengths. After applying the IPRF, we measured a decrease in the means of the standard deviations of 10% and 40% respectively for the G206 and G141 grisms. For each pixel, the response function in wavelength used to flat-field the spectra was determined by interpolating the narrow band flat-fields ($\sim$ 1% $\Delta\lambda/\lambda$) obtained as part of the standard NICMOS Cycle 7 calibration program. The inverse sensitivity curves (used by Nicmoslook to convert the spectral flux into mJy units) were obtained for each grism from observations of the calibrator stars P330E and G191B collected during the June 1998 "Camera-3 campaign". The intensities of the individual G206 spectra were adjusted in order to minimize the scatter in our data-set, and the 1-sigma errors represent the residual dispersion after correction. Comparison of the G141 and G206 spectra shows a mismatch in the overlap region, and we estimate the G206 flux to be 12% higher than the G141 flux after calibration. Using recent ground-based observations of Pluto carried-out by Owen *et al.* (1993) and recalibrated in geometric albedo by Roush *et al.* (1996), we find that the G141 grism calibration is best matched by the ground-based results, giving geometric albedoes of $p \sim 0.55$ and $p \sim 0.7$ at 1.9μm for the minimum and maximum of Pluto's lightcurve respectively. The precision of the flux calibration returned by the G141 grism is higher because its lower background makes the extraction of the photometric calibrators more accurate. We therefore selected the G141 grism as the reference for our photometric calibration. Our spectra of Pluto and Charon were then divided by the spectra of the solar analog star P330E (which were extracted using

Nicmoslook as described above). After correction of our spectra for the solar spectrum, we calibrated the spectra of Pluto and Charon in geometric albedo using the solar flux given by Labs and Neckel (1968) and the radii for Pluto (1151 ±4km) and Charon (591 ±5km) determined by Reinsch *et al.* (1994). An independent reference for the solar flux (Thekekara 1973) was used and returned the same calibration values.

4. Results and discussion

Figure 2 shows the calibrated NICMOS spectra of Pluto and Charon obtained for the two dates of June 11 and 14, 1998. The spectra have been slightly smoothed (convolution with a 2-pixel wide Gaussian) in this figure in order to make their comparison easier. The original spectra with error bars are presented later, along with the modeling results in section 4.2.2.

4.1. Pluto

The focus of this paper being Charon, we will not provide a detailed model and discussion for the case of Pluto (Fig. 2-A) and will refer to Douté *et al.* (1999) for recent modeling of Pluto's spectra. Nevertheless, we will note, as a proof of the validity of the extraction procedure described above, that *(i)* the two grism spectra are self-consistent in the [1.60-1.85]μm overlap region, and *(ii)* there is excellent agreement between our NICMOS spectra and the higher-resolution spectra obtained by Douté *et al.* (1999). The strong bands of methane ice are clearly visible as well as the 2.15 μm dip due to N_2, particularly for the spectrum that corresponds to minimum of Pluto's lightcurve. Comparison of our spectra at both lightcurve minimum and maximum, with the higher resolution ground-based spectra obtained at UKIRT by Cruikshank *et al.* (1997), also shows

an excellent agreement between the two data sets for the 1.9μm "continuum" region. At shorter wavelengths, we note that our determination of Pluto's albedo is slightly higher than reported by the UKIRT measurements. But comparison of the relative $\frac{1.22\mu m}{1.9\mu m}$ ratio of the CH_4 continuum between our calibrated NICMOS spectra and recent ground-based data obtained at Keck (Brown and Calvin 2000), confirms that the continuum level for the blue-end of the spectra is higher than previously reported. Table 3 presents the broad-band photometric measurements derived from our spectroscopic data-set for both observation dates. We measure a magnitude difference $\Delta_K \sim 0.1$ Mag between maximum and minimum of Pluto's lightcurve, which agrees with previous ground-based observations.

EDITOR: PLACE FIGURE 2 HERE.

4.2. Charon

Fig. 2-B compares the calibrated spectra of the leading and trailing hemispheres of Charon and shows that *(i)* water ice appears to be in its crystalline state on both hemispheres, *(ii)* the HST/NICMOS geometric albedo is slightly higher than reported from analysis of the mid-80's mutual occultation events, and *(iii)* spectral features characteristic of species like hydrogen cyanid (HCN), or more probably ammonia hydrate ($NH_3 \cdot H_2O$), are present in the spectrum of Charon's leading side.

4.2.1. Crystalline ice versus amorphous

The spectra of Fig. 2-B show the 1.65μm spectral feature characteristic of crystalline water ice for both trailing and leading hemispheres of the satellite. Water ice has also been found in its crystalline state on the surface of the large satellites of Uranus (Grundy

et al. 1999). This suggests that resurfacing processes can occur in the outer solar system at a faster rate than required for water ice to turn into its amorphous state under the action of solar irradiation. A possible mechanism proposed by Brown and Calvin (2000), implicates vaporization of the outermost layers of water ice on Charon by micrometeorite bombardments and recondensation of this ice in its crystalline state over the surface of the satellite.

Fig. 2-B also shows differences between the spectral response of Charon's leading and trailing hemispheres. In particular, the spectral slope at short-wavelengths is stronger for the leading side, which could be directly linked to the nature of the neutral absorber in surface. Also, the depth of the 1.55μm water band is shallower for the leading side, which might indicate hemispheric variations in the grain size distribution of water ice, although we would expect a similar behavior for the 2.02μm water band. The 2.21μm feature in the spectrum of Charon's leading side will be discussed later in section 4.2.3.

EDITOR: PLACE TABLE 3 HERE.

4.2.2. Geometric albedo of Charon

Table 3 presents the broad-band photometric measurements derived from the spectra of Charon's trailing and leading sides. The K-band magnitude difference between both hemispheres is within the uncertainty of our measurements, confirming that leading and trailing sides of Charon have a similar brightness. The calibration of our HST/NICMOS spectra returns a value of Charon's geometric albedo of $p \sim 0.42 \pm 0.05$ in the 1.8 μm water continuum region (Fig. 2-B), which is slightly higher than the $p \sim 0.34 \pm 0.05$ measurement (Roush *et al.* 1996) derived from the mid-80's mutual events (although both error bars overlap). The difference in Charon's geometric albedo reported in this paper is small but

larger than the uncertainty of the NICMOS grism-calibration which is estimated to be in the 5-10% range (Freudling and Pirzkal 1998). Furthermore, the good agreement between the HST/NICMOS determination of Pluto's geometric albedo (Fig. 2-A) and earlier ground-based measurements, validates the absolute calibration of our data. This sensibly higher determination of Charon's albedo cannot be produced by residual contamination from the planet. Indeed, the immediate consequence would be to underestimate Pluto's albedo whereas our measurements agree with the ground-based results. The slightly higher NICMOS albedo is consistent (within the error bars) with the earlier results and might simply reflects larger uncertainties than previously estimated in Charon's diameter and in the photometric calibration of the mutual events data. If the increase in albedo is real, then it might suggest time variable phenomena over Charon, like seasonal changes occurring while the system is moving away from the sun. Also, the satellite is now observed with an aspect angle ten degrees larger than during the 1987 mutual events, presenting a slightly larger apparent cross-section of its southern polar region. The present geometry could contribute to an increase in albedo if the southern polar region is made of material displaying a high reflectivity at these wavelengths. Comparison with other icy satellites of the outer solar system is possible. Near-infrared spectroscopy of the large satellites of Saturn returns geometric albedo measurements in the range $p \sim 0.2$ (Hyperion) to $p \sim 1.0$ (Mimas). The NICMOS observations show that Charon's albedo of $p \sim 0.4$ at 1.8μm is very similar to the albedo of Iapetus' trailing side, which is typical of a "dirty-ice" composition. Figure 3 shows the result of modeling the reflectance spectra of Charon leading and trailing hemispheres with an intimate mixture of ($\sim 90\%$) of crystalline water ice (30μm grain size) and $\sim 10\%$ of spectrally blue component, the later being required to match the continuum level at short wavelengths. Both spectra of Charon are reasonably well matched by the spectrum of pure water ice, except for the 2.21μm band and the short-wavelength region (Charon's trailing side). The modeling results do not require the addition of CO_2 ice or

CH_4 ice to improve the final fit.

EDITOR: PLACE FIGURE 3 HERE.

4.2.3. The leading hemisphere of Charon

The HST/NICMOS spectrum of Charon's leading side (Fig. 3-B) is identical to the spectrum of the same side of the satellite obtained at Keck by Brown and Calvin (2000). It displays the same 2.21μm spectral feature that was attributed to the presence of ammonia hydrate on the surface of the satellite. This additional and independent detection of the 2.21μm band suggests that this spectral feature is real, and rules out the possibility that it could be produced by residual contamination from Pluto.

EDITOR: PLACE FIGURE 4 HERE.

The first obvious candidate for this 2.21μm feature is CH_4 ice itself. Although we do not expect methane ice to be still present over Charon's surface, we nevertheless modeled the spectrum of Charon's leading side (Fig. 4) with an intimate mixture of water ice ($\sim$78%; 30μm grain size), methane ice ($\sim$15%; 30μm grain size) and $\sim$ 7% of the spectrally blue compound described earlier. The model presented in Fig. 4 shows that adding methane ice to the mixture does not provide a good match of the features observed in the spectrum of Charon's leading side. The small amounts of methane used in the model can reproduce the depth of the 2.21μm feature while allowing the two-band complex in the [1.7-1.8]μm region to be at the noise level of the spectrum. But further comparison shows that: *(i)* the deeper bands of methane longward of 2.3μm are too strong to match our data-set, and *(ii)* the 2.2μm band of methane is too narrow to provide a good fit of the 2.21μm feature.

EDITOR: PLACE FIGURE 5 HERE.

Other possible candidates display an absorption feature near 2.2μm. Figure 5 shows the reflectance spectra of ammonia hydrate for various weight concentration of NH_3, as well as the spectrum of hydrogen cyanid (HCN). Based only on their respective "history" of detections, HCN would be a stronger candidate than NH_3. Indeed, ammonia ice has never been securely detected yet on any other satellite of the solar system while HCN has been found several times in cometary material as well as in some star forming regions. In addition, HCN has a sublimation temperature of 87K and can be trapped in water ice quite efficiently to be released solely by evaporation of the water ice (Notesco and Bar-Nun 1997). On the other hand, near-infrared spectra of Europa's trailing side (Brown *et al.* 1988) recorded in 1980 and 1985 showed several bands at 1.8μm, 2.21μm and 2.32μm that were associated to ammonia ice. The same absorption features could not be detected in subsequent observations of Europa obtained in 1986, suggesting that, if real, the presence of ammonia on Europa had to be associated with transient phenomena occurring at the surface of the satellite. Such events are supported by high-spatial resolution images of the satellite obtained with the Galileo spacecraft, which showed distinct surface features that could be produced by the sublimation of volatiles such as ammonia ice (Greeley *et al.* 1998). Figure 5 shows the comparison of the reflectance spectra of HCN and $NH_3{\cdot}H_2O$ (3% of NH_3) with the spectra of the trailing and leading hemispheres of Charon. Although other absorption features are present in our spectrum of Charon's leading side (like for instance a dip at 1.77μm and a marginal feature at 2.3μm), only the band at 2.21μm is clearly emerging above the noise level of our data. We will note that, except for the 2.21μm band, HCN and NH_3 have most of their absorptions coinciding with the strong bands of water ice, making their detection particularly difficult. We will therefore limit our discussion to the 2.2μm region of the spectrum. Figure 6 shows also that NH_3 displays

a narrower absorption at 2.21μm band than HCN, matching better the feature observed in the spectrum of Charon's leading side. For this reason, we consider ammonia hydrate a better candidate than HCN to explain the 2.21μm band, although higher S/N spectra are needed to definitively identify the compound responsible for this absorption. Also, in spite of the fact that the detection of an absorption feature near 2.3μm is more marginal than the strongest 2.21μm band, it could correspond to a similar absorption detected in the spectrum of the trailing side of Europa (Brown *et al.* 1988), which was attributed to the presence of ammonia hydrate in surface.

EDITOR: PLACE FIGURE 6 HERE.

Several cases can be discussed in which compounds (other than water ice) present on Charon's leading side are either endogenic or exogenic. Geological activity such as cryovolcanism, producing flow of pristine volatile material through cracks, could transport interior ices to the surface of the satellite. Charon's surface cannot retain any volatiles over the age of the solar system, but nitrogen ice could still be present below the external layer. Such a mechanism would be possible only if ammonia is produced from nitrogen at a faster rate than needed for the volatiles to sublimate, but even in this case, the apparent concentration of ammonia ice on the leading side of Charon would remain to be explained. Also, any tidal heating of Charon that could be responsible for a volcanic-type activity similar to Triton's, is suspected to have stopped long ago given that Pluto and Charon are both rotationally locked and tidally relaxed.

Alternatively, new species can be produced on Charon from bombardment of its surface by ions escaping from Pluto. Owen *et al.* (1993) estimated that N_2 constituted more than 99% of Pluto's atmosphere. Given Pluto's nitrogen-rich surface and atmosphere, the escape of N_2 is likely to happen simultaneously with the escape of CH_4. The escape rate

of N_2 is driven by both the atmospheric temperature ($\sim$ 106K, Yelle and Lunine 1989) and the CH_4 mixing ratio, and varies seasonally with the heliocentric distance of Pluto. The 9.8 ev energy level required to dissociate molecular nitrogen (Allen 1993) corresponds to the regime of ionizing extreme UV radiations with wavelengths shorter than 1260Å. This energy range contains the intense Lyman-α emission line (λ = 1216Å) of the solar chromosphere which produces a flux of $3.4 \cdot 10^{12}$ photons/m^2/s at 30 AU from the sun and can dissociate molecular nitrogen into N^+ ions (N_2^+ recombines rapidly). The simplest mechanism to form ammonia on one side of the satellite would be to have N_2/N^+ escaping from Pluto's atmosphere and impacting the leading side of Charon because of its orbital motion. Whipple *et al.* (1989) showed that a portion of the molecules escaping from Pluto's atmosphere would be trapped in the Pluto-Charon system, similar to the interaction occuring in the case of a close binary star system. Compositional differences between leading and trailing hemispheres of satellites have already been observed in our solar system and usually implicate hemispheric resurfacing by redeposition of dust or ice released by a nearby body. The dark leading hemisphere of Iapetus is a good illustration of resurfacing processes implicating the action of an external source, in this case, the nearby satellites Hyperion (Buratti *et al.* 1999) or Phoebe. The nature of the plasma surrounding Charon is mainly controlled by the existence (or absence) of a magnetosphere around Pluto, which is driven by both the degree of magnetization of the planet and its atmospheric escape rate. If Pluto maintains a weak remnant magnetization (comparable to chondrite meteorites), the interaction of escaping ions from Pluto's atmosphere with the weak solar wind at 30 AU, would produce a magnetosphere extending beyond the orbit of Charon (Bagenal *et al.* 1997). The plasma surrounding Charon would then be controlled by ions escaping from the planet. However, with the locked system defined by Pluto, its magnetic field, and Charon, it is not clear that such a mechanism would favor the accumulation of ions over the leading hemisphere of Charon.

Is the production of NH_3 from bombardment of water ice with N^+ likely to happen ? Laboratory experiments to measure the effect of ion irradiation of an icy surface (Strazzulla 1998) show that the implantation of reactive ions over the surface of planetary satellites could produce new molecular species that are not native to those surfaces. But Strazzula and Palumbo (1998) also showed that bombardment of a mixture of water and ammonia ices by energetic ions decreases the concentration of ammonia ice. In addition, the binding energy of NH_3 is 2.2 times smaller than N_2 and it is therefore photolytically destroyed quite rapidly. An estimation of its production and dissociation rates is needed to test if ammonia ice can be preserved from rapid dissociation. If ammonia ice is present on Charon, it is probably formed as ammonia clathrate and H_2O molecules could provide some shielding once the upper layers are depleted of NH_3. Indeed, if the water ice on Charon is mixed with small amount of CH_4 (escaped from Pluto's atmosphere), its irradiation by solar UV would quickly form a photolytic "skin" of organics a few microns thick. Even a very small amounts of light hydrocarbons (which are excellent UV absorbers) on the surface would still allow the detection of the NH_3 bands in the near-infrared while providing shielding to protect NH_3 from rapid dissociation.

Much work still needs to be done in order to better understand the complex nature of Charon's surface. Additional spectra at higher spectral and spatial resolution will help to securely identify the compound(s) responsible for the absorption features observed in the spectrum of its leading side. Further observations at various rotational phases of the satellite will allow us to measure the spatial distribution of species other than water ice, and test whether the 2.21μm feature is also present in the spectrum of the Pluto-facing hemisphere of Charon. Also, laboratory experiments to measure the optical properties of

NH_3 ice need to be carried-out to model the recent spectra of Charon obtained from the ground and space, and the effect of bombardment of water ice by N^+/N_2 should be studied in more detail to quantify the effectiveness of this process to form ammonia hydrate on Charon.

The authors would like to thank Rodger Thompson and Marcia Rieke from the NICMOS IDT team and Wolfram Freudling and Norbert Prizkal from ST-ECF for the support provided with Nicmoslook. We are also grateful to Tobias Owen for his helpful comments on the manuscript, and Dale Cruikshank for providing the reflectance spectrum of HCN. This work was performed at the Jet Propulsion Laboratory, California Institute of Technology, under contract to the National Aeronautics and Space Administration.

Table 1. **Geometry of the Pluto-Charon system during the June 1998 "Camera-3 campaign"**

	June 11, 1998 13:01 (UT)[a]	June 14, 1998 14:56 (UT)[a]
Heliocentric distance (AU)	30.0684	30.0692
Geocentric distance (AU)	29.1049	29.1190
Sub-Earth latitude (deg)	-21.4	-21.3
Pluto's sub-Earth longitude (deg)	99.6 (max. lightcurve)	273.2 (min. lightcurve)
Charon's sub-Earth longitude (deg)	279.7 (trailing side)	93.2 (leading side)
Separation (")	0.908	0.917
Charon's position angle (deg)	169.95	347.65
Spectral separation (pixel)	2.55 (=0.517")	2.70 (=0.548")

[a]Time at beginning of G206 series

Table 2. **Grism-observation parameters**

	G141 grism	G206 grism
Spectral coverage (μm)	[1.1–1.9]	[1.4-2.5]
Number of exposures	2	12
Total exposure time (s)	639.9	767.4
NICMOS sequence	Step64	Step16

Table 3. **Near-infrared photometry of Pluto-Charon**[a]

	PLUTO			CHARON		
	J_{mag}[b]	H_{mag}[c]	K_{mag}[d]	J_{mag}[b]	H_{mag}[c]	K_{mag}[d]
June 11, 1998	12.69±0.01	12.66±0.01	13.09±0.04	14.74±0.03	14.70±0.02	14.81±0.12
June 14, 1998	12.83±0.02	12.81±0.02	13.19±0.04	14.70±0.04	14.63±0.04	14.81±0.10

[a]These measurements are derived from the spectra in Fig. 3. The error bars in magnitude reflect only the 1-σ uncertainty plotted in the figure. The absolute photometric accuracy of the grisms in NIC3 is itself evaluated to be in the 5-10% range.

[b]J: [1.15-1.35]μm. 0-mag=1576.2 Jy for λ_{eff}=1.25μm.

[c]H: [1.50-1.80]μm. 0-mag=1018.6 Jy for λ_{eff}=1.65μm.

[d]K: [2.00-2.40]μm. 0-mag=672.8 Jy for λ_{eff}=2.20μm.

REFERENCES

Allen, C. W. 1973, Astrophysical Quantities, The Athlone Press, 47

Bagenal, F., Cravens, T. E., Luhmann, J. G., McNutt, R., L., and Cheng, A. F. 1997, Pluto and Charon, S. A. Stern and D. J. Tholen, Univ. Ariz. Press, 523

Brown, M. E., and Calvin, W. M. 2000, Science, 287, 107

Brown, R. H., Cruikshank, D. P., Tokunaga, A. T., Smith, R. G., and Clark, R. G. 1988, Icarus, 74, 262

Buie, M. W., and Fink, U. 1987, Icarus, 70, 483

Buie, M. W., and Grundy, W. M. 2000, submitted to Icarus

Buie, M. W., Tholen, D. J., and Horne, K. 1992, Icarus, 97, 211

Buie, M. W., Cruikshank, D. P., Lebofsky, L. A., and Tedesco, E. F. 1987, Nature, 329, 522

Buratti, B. J., Hicks, M. D., Tryka, K. A., Sittig, M., and Newburn Jr., R. 1999, BAAS, DPS Meeting. 13.03

Cruikshank, D. P., Pilcher, C. B., and Morrison, D. 1976, Science, 194, 835.

Cruikshank, D. P., Roush, T. L., Moore, J. F., Sykes, M., Owen, T. C., Bartholomew, M. J., Brown, R. H., and Tryka, K. A. 1997, Pluto and Charon, S. A. Stern and D. J. Tholen, Univ. Ariz. Press, 221

Cruikshank, D. P., Allamandola, L. J., Hartmann, W. K., Tholen, D. J., Brown, R. H., Matthews, C. N., and Bell, J. F. 1991, Icarus, 94, 345

Davies, M. E., Abalakin, V. K., Bursa, M., Lieske, J. H., Morando, B., Morrison, D., Seidelmann, P. K., Sinclair, A. T., Yallop, B., and Tjuflin, Y. S. 1996, Celestial mechanics & dynamical astronomy, 63, 127

Douté, S., Schmitt, B., Quirico, E., Owen, T. C., Cruikshank, D. P., de Bergh, C., Geballe, T. R., and Roush, T. L. 1999, Icarus, 142, 421

Dumas, C., Terrile, R. J., Brown, R. H., and the NICMOS IDT team. 1999, Pluto and Triton Conference Abstracts, Lowell Observatory Sep. 23-24, 1999, Flagstaff, AZ

Freudling, W., and Pirzkal, N. 1998, NICMOS and the VLT Conference Proceed., 47

Greeley, R., Sullivan, R., Klemaszewski, J., Homan, K., Head, J. W. III, Pappalardo, R. T., Veverka, J., Clark, B. E., Johnson, T. V., Klaasen, K. P., Belton, M., Moore, J., Asphaug, E., Carr, M. H., Neukum, G., Denk, T., Chapman, C. R., Pilcher, C. B., Geissler, P. E., Greenberg, R., and Tufts, R. 1998, Icarus, 135, 4

Grundy, W. M., Buie, M. W., Stansberry, J. A., Spencer, J. R., and Schmitt, B. 1999, Icarus, 142, 536

Jewitt, D. 1994, AJ, 107, 372

Labs, D., and Neckel, H. 1968, Zeitschrift für Astrophysik, 69, 1

Lauer, T. R. 1999, PASP, 111, 1434

Lellouch, E., Laureijs, R., Schmidt, B., Quirico, E., de Bergh, C., Crovisier, J., and Coustenis, A. 1998, BAAS, 30, 1061

Marcialis, R. L., Rieke, G. H., and Lebofsky, L. A. 1987, Science, 237, 1349

McCarthy, P. J., Yan, L., Freudling, W., Teplitz, H. I., Malumuth, E. M., Weymann, R. J., Malkan, M. A., Fosbury, R. A. E., Gardner, J. P., Storrie-Lombardi, L. J., Thompson, R. I., Williams, R. E., and Heap, S. R. 1999, ApJ, 520, 548

Notesco, G., and Bar-Nun, A. 1997. Icarus, 126, 336

Owen, T. C., Roush, T. D., Cruikshank, D. P., Elliot, J. L., Young, L. A., de Bergh, C., Schmidt, B., Geballe, T. G., Brown, R. H., and Bartholomew, M. J. 1993, Science, 261, 745

Park, S., and Schowengerdt, R. 1983, Comp. Vis. Graph. Image Proc., 23, 256.

Pirzkal, N., and Freudling, W. 1998, NICMOS and the VLT Conference Proceed., 55

Reinsch, E. M., Burwitz, V., and Festou, M. C. 1994, Icarus, 108, 209

Roush, T. L., Cruikshank, D. P., Pollack, J. B., Young, E. F., and Bartholomew, M. J. 1996, Icarus, 119, 214

Roush, T. L. 1994, Icarus, 108, 243

Stern, S. A., Trafton, L. M., and Gladstone, G. R. 1988, Icarus, 75, 485

Stern, S. A., Buie, M. W., and Trafton, L. M. 1997, AJ, 113, 827

Strazzulla, G. 1998, Solar system ices, B. Schmidtt, C. de Bergh, M. Festou, Kluwer Academic Publishers, 281

Strazzulla, G., and Palombo, M. E. 1998, Planet. Space Sci., 46, 1339

Thekekara, M. P. 1973, Sol. Energy 14, 109

Thompson, R. I., Rieke, M., Schneider, G., Hines, D.C., and Corbin, M. 1998, ApJ, 492, 95

Tryka, K., Brown, R. H., Cruikshank, D. P., Owen, T. C., Geballe, T. R., and de Bergh, C. 1994, Icarus, 112, 513

Whipple, A. L., Trafton, L. M., and Stern, S. A. 1989, BAAS, 21, 982

Yelle, R. V., and Lunine, J. I. Nature, 339, 228

Young, L. A., Elliot, J. L., Tokunaga, A., de Bergh, C., and Owen, T. C. 1997, Icarus, 127, 258

Young, E. F., Galdamez, K., Buie, M. W., Binzel, R. P., and Tholen, D. J. 1999, AJ, 117, 1063

Fig. 1.— Cross-section of a rebinned G206 spectrum of Pluto-Charon along the spatial direction (y-axis of the detector). The original profile is noted with blue diamonds symbols while the synthetic profile of $(Pluto + Charon)$ is noted in solid red line. The residual of the fit, $(original\ profile - synthetic\ profile)$, is represented with a black solid line. For each original image, two synthetic images are produced by fitting the individual contributions of Pluto and Charon along the detector columns (3 iterations of the fitting algorithm). The synthetic images are then used to extract the individual spectrum of Pluto and Charon.

Fig. 2.— G141 and G206 spectra of Pluto (A) and Charon (B) obtained during the "Camera-3 Campaign" of June 1998. The species responsible for the absorption bands detected in our spectra are noted on the figures. Near-infrared spectroscopy of Charon shows that the 1.65μm feature of crystalline water ice is visible for both the leading and trailing sides. The 2.21μm absorption reported from Keck observations of Charon by Brown and Calvin (2000) is visible in the HST/NICMOS spectrum, but for the leading hemisphere only. Whatever compound (NH_3 ?) is responsible for this absorption, it is more abundant on the leading side of the satellite than on its trailing side.

Fig. 3.— Hapke modeling of the spectra of the trailing (A) and leading (B) hemispheres of Charon using an intimate mixture of water ice (40K) and a blue component ($< 10\%$) to adjust the continuum. The best matches are obtain for water ice grain sizes of $\sim$30μm. The $\pm 1\sigma$ error bars plotted with the spectra correspond the standard deviation of the spectral data-set (residual scatter) after calibration and division by the spectra of a solar analog. Deviation of the spectra from the models show that the surface composition of Charon is probably more complex than pure water ice.

Fig. 4.— Modeling of the spectrum of Charon's leading side with an intimate mixture of water and ammonia ices. While the model fits nicely the depth of the 2.21μm feature, the methane bands longward of 2.3μm are too deep to fit our data-set, ruling out the possibility that methane ice is the compound responsible for the 2.21μm band observed in the spectrum of Charon's leading side.

Fig. 5.— Reflectance spectra of possible candidates for the 2.21μm absorption feature. The upper spectrum is of an anhydrous HCN polymer (Cruikshank *et al.* 1991) while the 4 other spectra are of a mixture of water ice (crystalline) and ammonia ice for weight abundances of 1%, 3%, 10% and 30% of NH_3 (Brown *et al.* 1988). Note the increasing depth of the strong ammonia band at 2.21μm with increasing amount of ammonia ice in the $NH_3{\cdot}H_2O$ mixture.

Fig. 6.— Comparison of the band positions between the spectra of hydrogen cyanid (HCN) and ammonia hydrate ($NH_3{\cdot}H_2O$ for 3% of ammonia), and the calibrated spectra of Charon's leading (L) and trailing (T) hemispheres. The spectrum of the trailing side has been shifted downward by 0.15 unit while the reflectance spectra of HCN and $NH_3{\cdot}H_2O$ are overplotted with respective offsets of 0.35 and 0.6 units. The red solid vertical line mark the position of the 2.21μm band visible only in the spectrum of Charon's leading side. Both NH_3 and HCN display an absorption at 2.21μm similar to the absorption present in the spectrum of Charon's leading side but the profile of the ammonia hydrate band matches better the 2.21μm feature than HCN. The marginal 2.3μm absorption in the spectrum of Charon's leading side could correspond to a shallower band in the spectrum of ammonia hydrate (represented by the dashed line), but better S/N spectra are needed in order to clearly identify the specy responsible for the absorptions observed in the spectrum of Charon's leading side.

Figure 1

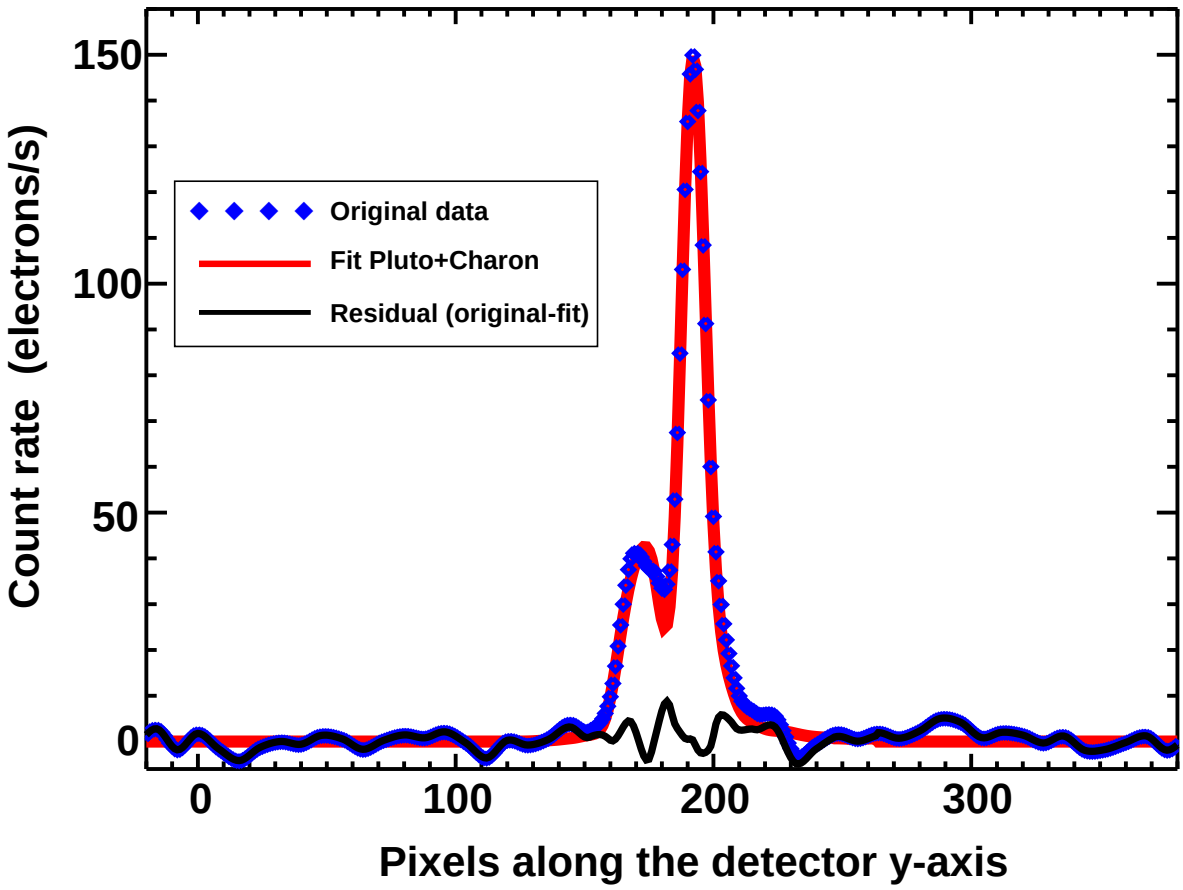
150
100
50
0
Count rate (electrons/s)
Original data
Fit Pluto+Charon
Residual (original-fit)
0
100
200
300
Pixels along the detector y-axis

Figure 2

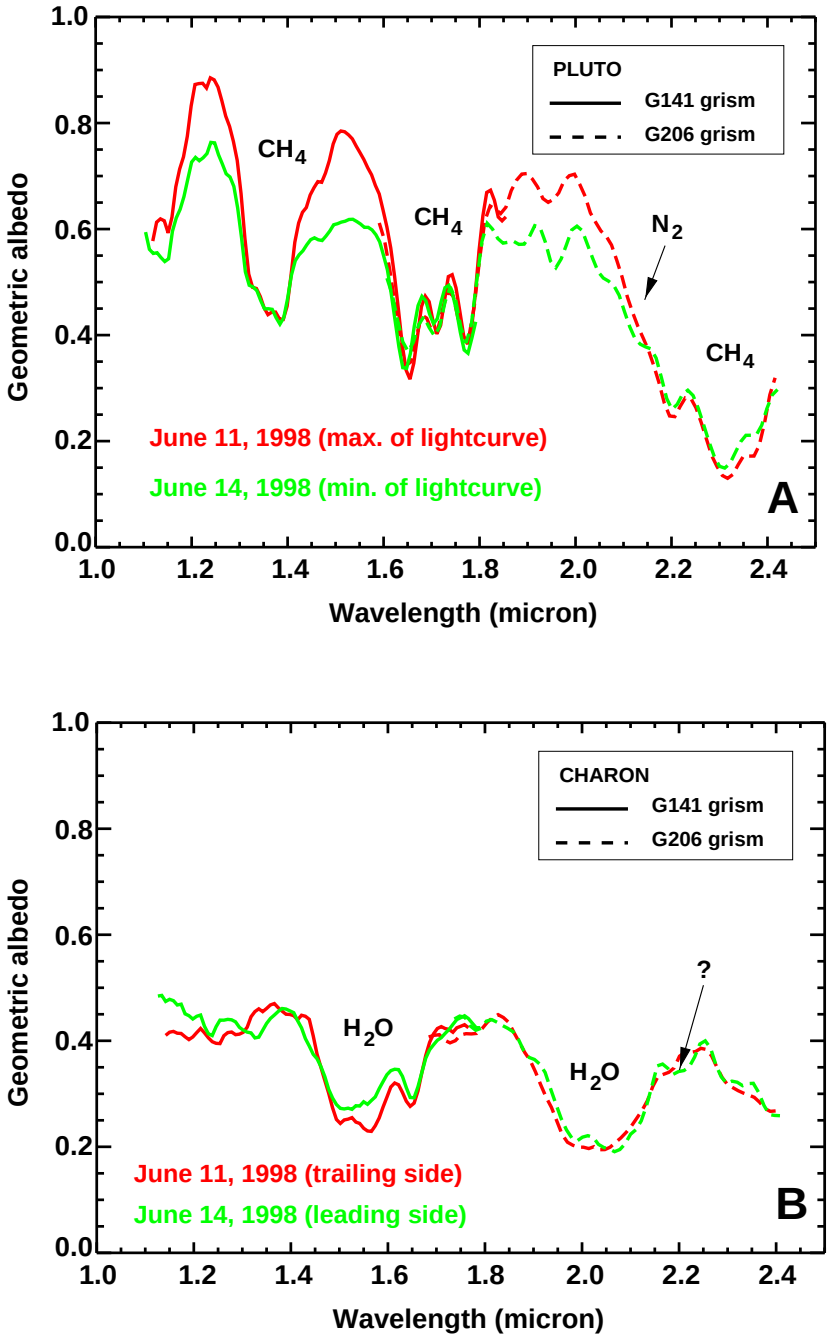
PLUTO
G141 grism
G206 grism
CH4
CH4
N2
CH4
June 11, 1998 (max. of lightcurve)
June 14, 1998 (min. of lightcurve)
A
Geometric albedo
Wavelength (micron)
CHARON
G141 grism
G206 grism
H2O
H2O
?
June 11, 1998 (trailing side)
June 14, 1998 (leading side)
B
Geometric albedo
Wavelength (micron)

Figure 3

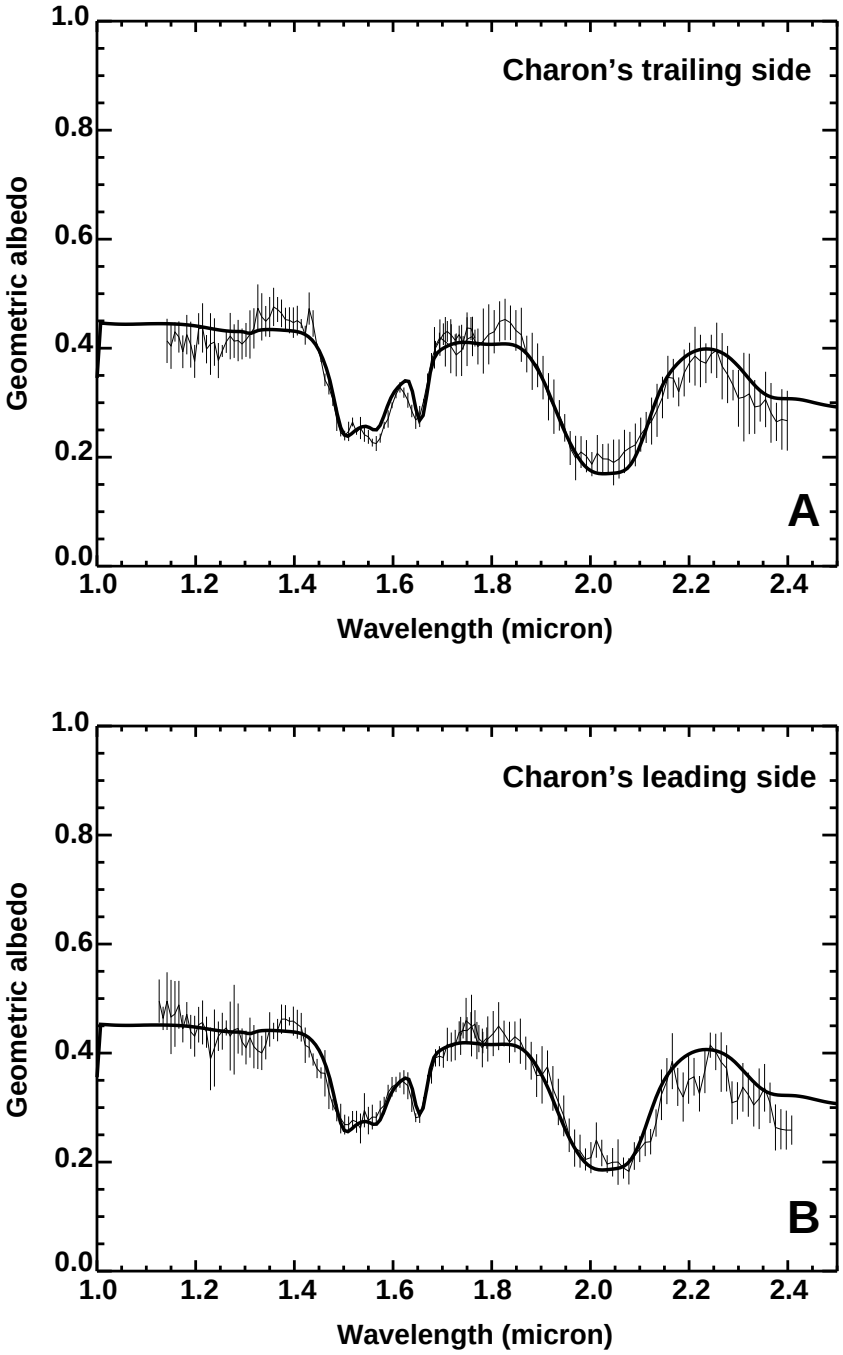
Charon's trailing side
A
Geometric albedo
Wavelength (micron)
1.0
0.8
0.6
0.4
0.2
0.0
1.0
1.2
1.4
1.6
1.8
2.0
2.2
2.4
Charon's leading side
B
Geometric albedo
Wavelength (micron)

Figure 4

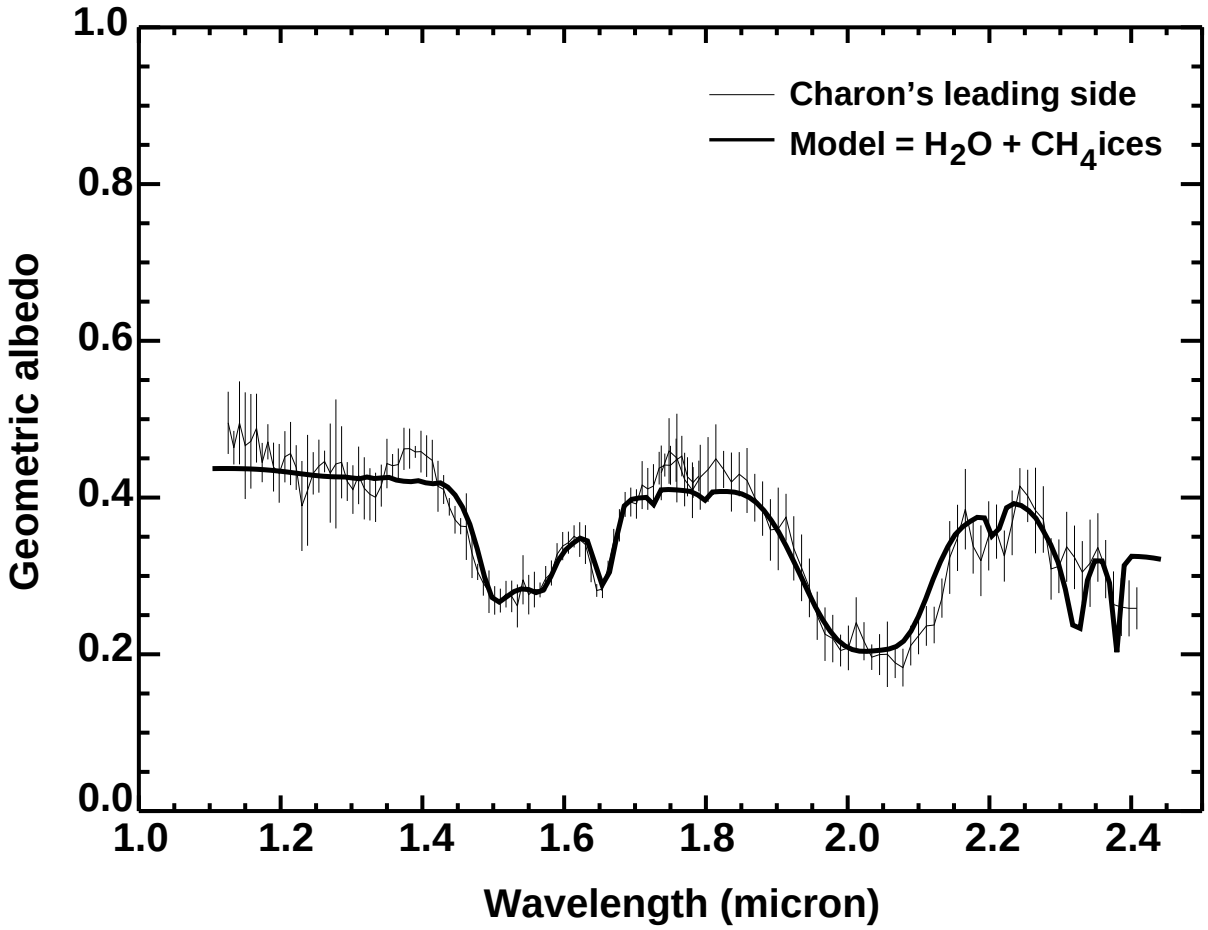
Charon's leading side
Model = H2O + CH4ices
Geometric albedo
Wavelength (micron)
1.0
0.8
0.6
0.4
0.2
0.0
1.0
1.2
1.4
1.6
1.8
2.0
2.2
2.4

Figure 5

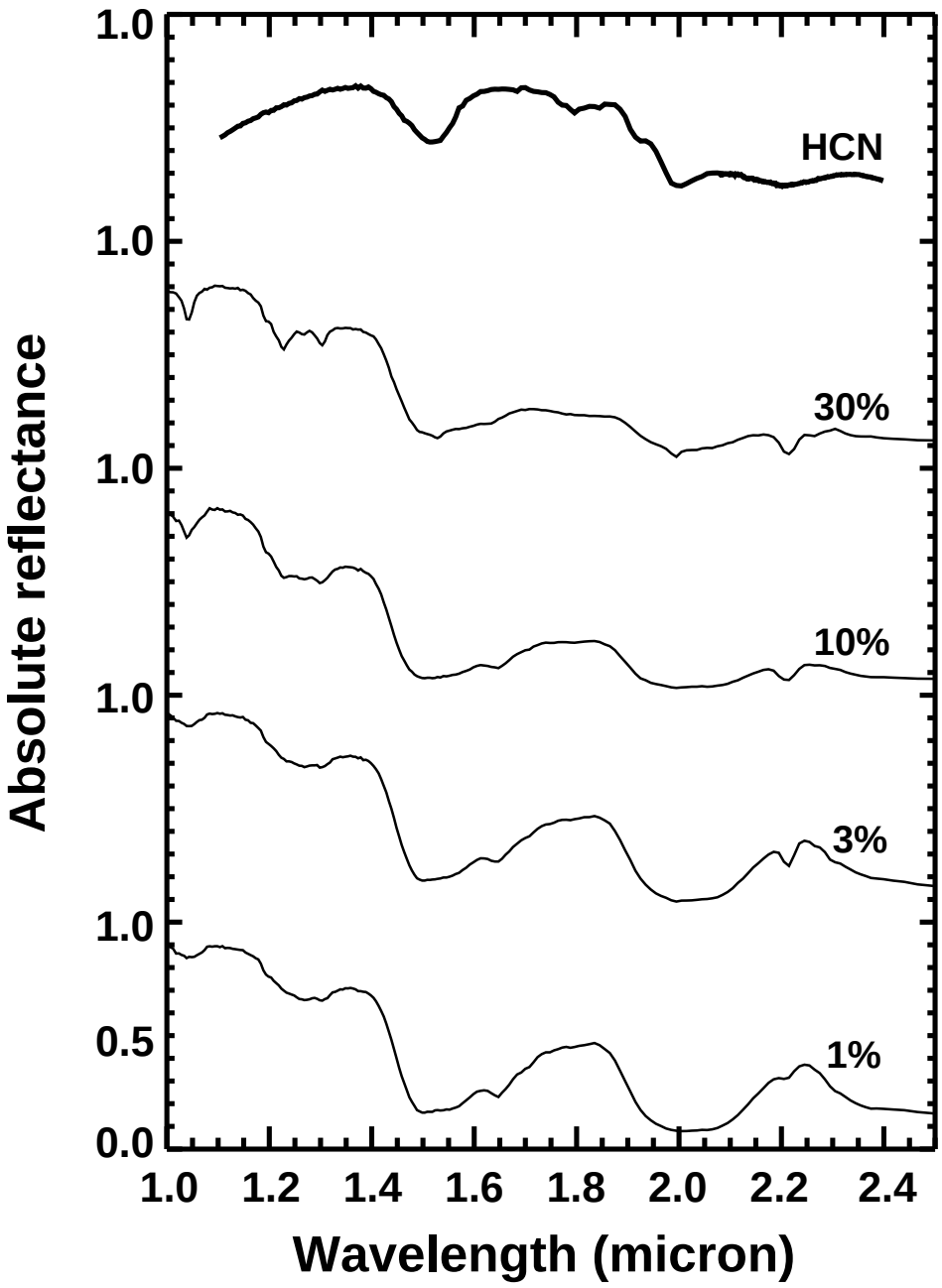
1.0
1.0
1.0
1.0
0.5
0.0
HCN
30%
10%
3%
1%
Absolute reflectance
1.0
1.2
1.4
1.6
1.8
2.0
2.2
2.4
Wavelength (micron)

Figure 6

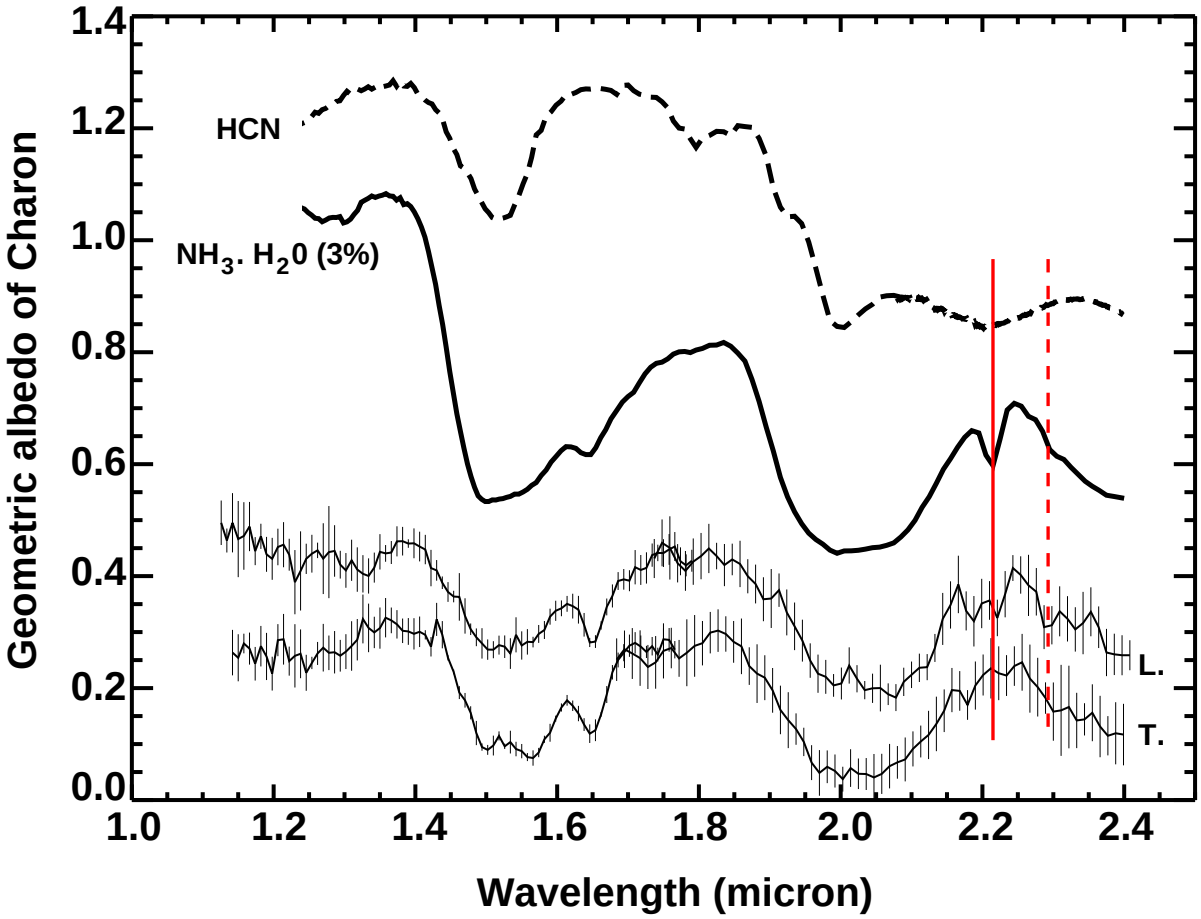
Geometric albedo of Charon
Wavelength (micron)
HCN
NH3. H20 (3%)
L.
T.
1.4
1.2
1.0
0.8
0.6
0.4
0.2
0.0
1.0
1.2
1.4
1.6
1.8
2.0
2.2
2.4